AGU PUBLICATIONS

JGR

Journal of Geophysical Research: Solid Earth

RESEARCH ARTICLE

10.1002/2013JB010314

Key Points:
- One percent melt in the LVL above transition zone
- Same melt volume fraction in subduction and plume settings
- Electrical conductivity better matches observations with silicate melts

Correspondence to:
S. Hier-Majumder,
Saswata.Hier-Majumder@rhul.ac.uk

Citation:
Hier-Majumder, S., E. B. Keel, and A. M. Courtier (2014), The influence of temperature, bulk composition, and melting on the seismic signature of the low-velocity layer above the transition zone, *J. Geophys. Res. Solid Earth*, *119*, 971–983, doi:10.1002/2013JB010314.

Received 29 APR 2013
Accepted 29 JAN 2014
Accepted article online 4 FEB 2014
Published online 22 FEB 2014

The influence of temperature, bulk composition, and melting on the seismic signature of the low-velocity layer above the transition zone

Saswata Hier-Majumder[1,2], Ellen B. Keel[3], and Anna M. Courtier[4]

[1]Department of Earth Sciences, Royal Holloway University of London, Egham, UK, [2]Department of Geology, Center for Scientific Computation and Applied Mathematical Modeling, University of Maryland, College Park, Maryland, USA, [3]Department of Mathematics and Statistics, James Madison University, Harrisonburg, Virginia, USA, [4]Department of Geology and Environmental Science, James Madison University, Harrisonburg, Virginia, USA

Abstract We report a new technique to describe seismic velocity and impedance anomalies atop a seismic low-velocity layer (LVL) at 350 km depth. We model shear wave speed reductions detected with Ps conversions beneath the Hawaiian Islands and negative impedance contrasts detected with *ScS* reverberations beneath the Coral Sea in the South Pacific, by varying the bulk solid composition, reference potential temperature, dihedral angle of melt, and melt composition. For a given bulk solid composition, the effects of elevated temperature and melt volume fraction on the seismic properties trade off with one another. At a given temperature, the calculated melt volume fraction is nearly insensitive to variations in the bulk solid composition. A low volume fraction of low dihedral angle melts mimics the seismic signature of a higher volume fraction of high dihedral angle melts. Despite stronger lateral variations in the LVL structure beneath Hawaii compared to the Coral Sea, both regional averages are similar. For a basalt volume fraction of 0.2 and a dihedral angle of 10°, we estimate regional averages of 1.1 ± 0.8 vol % melt at a depth of 350 km beneath the Hawaiian Islands for a reference potential temperature of 1800 K and 1.2 ± 0.005 vol % melt at a depth of 350 km beneath the Coral Sea region for a reference potential temperature of 1500 K. Our model of the seismic signal is unable to distinguish between melt compositions of mid-ocean ridge basalt and carbonated peridotite melts at such small melt volume fractions.

1. Introduction

The Earth's upper mantle is a dynamic region. Among other features in the mantle, a number of recent studies identify the presence of a low-velocity layer (LVL) in the deep upper mantle, directly atop the mantle transition zone (MTZ) [e.g., *Courtier and Revenaugh*, 2007; *Vinnik and Farra*, 2007; *Revenaugh and Sipkin*, 1994; *Tauzin et al.*, 2010; *Gao et al.*, 2006; *Jasbinsek and Dueker*, 2007; *Huckfeldt et al.*, 2013]. While *Tauzin et al.* [2010] argue that the layer is likely global in nature, its localized presence has been defined in a number of regions, including beneath the Coral Sea in the South Pacific [*Courtier and Revenaugh*, 2007] and the Hawaiian Islands [*Huckfeldt et al.*, 2013]. The key seismic signature of the LVL typically involves anomalous reductions in the shear wave speed and/or impedance contrast relative to global models (e.g., preliminary reference Earth model (PREM)) [*Dziewonski and Anderson*, 1981] at the upper boundary of the LVL. The thickness of the LVL is estimated to be up to 100 km [*Revenaugh and Sipkin*, 1994; *Song et al.*, 2004].

Anomalous shear wave speed and impedance contrast can be caused by changes in temperature, bulk composition, or partial melting within the LVL or by a combination of these factors. While increased temperature and partial melting typically lead to a reduction in shear wave speed, the influence of bulk solid composition varies within different parts of the mantle [*Xu et al.*, 2008]. In addition, for a given solid composition and temperature, partial melting can influence the shear wave speed through melt volume fraction, dihedral angle at the grain-melt interface, and the composition of the melt [*Hier-Majumder and Abbott*, 2010; *Wimert and Hier-Majumder*, 2012; *Hier-Majumder*, 2008; *Hier-Majumder and Courtier*, 2011]. Variations in melt composition are manifested as variations in the bulk modulus and density of the melt. A crucial part of understanding the nature of the LVL, therefore, is to simultaneously account for all of these sources of variation in the evaluation of the seismic signature. In this article, we present a combined analysis of observed shear wave speed, impedance, and topography along the top of the LVL [*Courtier and Revenaugh*, 2007; *Huckfeldt et al.*, 2013], which involves elastic properties of both the solid [*Xu et al.*, 2008] and the melt

[*Guillot and Sator*, 2007; *Ghosh et al.*, 2007], and microgeodynamic models of melt geometry [*von Bargen and Waff*, 1986; *Wimert and Hier-Majumder*, 2012] to infer the signatures of thermal, compositional, and melting-related anomalies.

Such an understanding of the lateral variations in the layer thickness and seismic properties along the LVL also has geodynamic implications. While the region beneath the Coral Sea is adjacent to a subduction zone, the Hawaiian Islands are located atop a mantle plume. These tectonic settings have contrasting thermal structure, volatile content, and mantle flow patterns. In addition to the properties of the LVL, variations in the MTZ thickness and topography along the 410 km discontinuity (the olivine-wadsleyite phase transition that marks the top of the MTZ) can be used to estimate the relative mantle potential temperature. Combined petrological and seismic methods indicate that the regional potential temperature in the Hawaiian Islands is near 1800 K [*Courtier et al.*, 2007b]. Combining the anticorrelation between transition zone thickness and regional potential temperatures posited by *Courtier et al.* [2007b] and the thickness of the MTZ beneath the Coral Sea region [*Courtier and Revenaugh*, 2007], the regional potential temperature in the Coral Sea region is likely near 1500 K. Comparing and contrasting the seismic signature of the LVL and the MTZ between these two different geodynamic settings provides some fundamental insights into the nature of the LVL and upper mantle dynamics.

If partially molten, observations of the LVL can provide some constraints on the existing models of volatile-induced melting in the deep upper mantle. For example, the transition zone water filter model of *Bercovici and Karato* [2003] suggests that hydrogen, trapped as point defects within nominally anhydrous wadsleyite, induces melting atop the MTZ upon pervasive upwelling across the 410 km discontinuity, as olivine has a lower solubility for hydrogen. If present, such a mechanism will generate a partially molten layer atop the MTZ. For a plume setting in this model, the solubility gap will diminish, and the partial melting will be largely suppressed due to locally higher temperatures. In a subduction zone, the partially molten layer will be dragged into the MTZ along with the subducting slab [*Leahy and Bercovici*, 2007]. As a result, the water filter model predicts the near absence of the LVL in a plume setting and a likely greater depth of occurrence in the subduction zone setting resulting in a thinner or even lens-shaped layer due to entrainment by the subducting slab. In another model, *Dasgupta and Hirschmann* [2010] suggest that the presence of carbonates can induce silicate melting at depths between 300 and 330 km for most of the mantle. In this model, however, the partial melting would take place at greater depths in a plume setting and possibly also in a subduction zone setting. In addition, melts bearing carbonate are marked by substantially high electrical conductivity. Once the melt volume fraction is estimated from modeling of the seismic observation, the resulting electrical conductivity can provide additional information on the melt composition.

In the following sections, we discuss the methods of data analysis and error estimates, present both station-specific and regionally averaged information on the various parameters, and discuss the implications for volatile-induced melting in the LVL. The numerical experiments were carried out using a suite of object-oriented Fortran 2003 libraries, named **MuMaP** (**Mu**ltiphase **Ma**terial **P**roperties, pronounced μ-map).

2. Methods

We report our methodology in two distinct steps: (1) the method for modeling the seismic observations (from Ps conversions and *ScS* reverberations) and (2) the algorithm for obtaining melt volume fraction from the observed shear wave speed. These steps are outlined in the following two subsections.

2.1. Processing Seismic Data

We use the data from *Huckfeldt et al.* [2013] to study the seismic signature of thermal, compositional, and melting anomalies beneath Hawaii. *Huckfeldt et al.* [2013] analyzed Ps conversions from the upper mantle and transition zone beneath 65 stations on and around the Hawaiian Islands. Rather than examining the Ps conversions at a single frequency, they conducted a detailed analysis of the frequency dependence of all observed features from 0.1 to 2.0 Hz at 0.1 Hz increments. Only observations that were consistent across a broad frequency range were considered confident observations. Further details of the method and results of the converted wave study are reported in *Huckfeldt et al.* [2013]. Mantle profiles beneath 27 of the 65 stations contained confident observations of both an LVL around 350 km depth and the 410 km discontinuity, which marks the top of the MTZ. We use seismic observations of the converted wave amplitudes and depths for both the LVL and 410 km discontinuity beneath each of the 27 stations that confidently reported those data.

To provide a comparison in another tectonic setting and with previous work, we also use MuMaP to model the properties of an LVL beneath the Coral Sea. *Courtier and Revenaugh* [2007] detected a negative impedance contrast at ~350 km depth in this region using *ScS* reverberations [*Revenaugh and Jordan*, 1991]. Previous efforts to analyze this LVL [*Hier-Majumder and Courtier*, 2011] modeled a regional average of the seismic results. Here we divide the seismic results into eight geographic source-receiver corridors—"paths" that cross the Coral Sea region in different orientations—in order to assess lateral variability and compare with the Hawaiian study. The eight corridors represent half of the corridors analyzed by *Courtier and Revenaugh* [2007] that resulted from 180 earthquakes recorded at 12 seismic stations; the additional corridors in the original study were in regions that did not detect an LVL. Further details of the method and results of the *ScS* reverberation study are reported in *Courtier and Revenaugh* [2007].

2.1.1. Calculating Shear Wave Speed From Observations

Two issues need to be addressed while modeling the observed Ps conversion results. The first issue arises from minor variations in the amplitude of the observed Ps conversions across different frequencies of converted waves. To address this issue, we averaged the converted wave amplitude in a frequency range from 0.1 to 0.5 Hz, where structure is less variable than at higher frequencies. The second issue arises from the variation in the strength of signal between different stations. We normalized the frequency-averaged amplitude atop the LVL at each station by the frequency-averaged amplitude at the 410 km discontinuity for the same station (defined as the "amplitude contrast"), thus filtering out the artificial signal strength variations from station to station. For the Ps conversion results, we can define two useful quantities,

$$R_{\mathrm{LVL}}^{\mathrm{norm}} = \frac{\text{Amplitude across LVL}}{\text{Amplitude across 410}} < 0, \tag{1}$$

where $R_{\mathrm{LVL}}^{\mathrm{norm}}$ is the normalized amplitude of the converted arrivals. We also define the normalized velocity contrast, η, as

$$\eta = \frac{V_S^{410} - V_S^{\mathrm{top}}}{V_S^{\mathrm{top}}} > 0, \tag{2}$$

where the superscripts "top" and "410" refer to the values of wave speeds just above and just below the top of the 410 km discontinuity in the PREM global seismic wave speed model [*Dziewonski and Anderson*, 1981]. If the shear wave speed immediately above the LVL is expressed by V_S^{norm} and immediately below the top of the LVL is the observed shear wave speed V_S^{obs}, then using the reference velocity contrast η and the normalized amplitude contrast $R_{\mathrm{LVL}}^{\mathrm{norm}}$, we get

$$V_s^{\mathrm{obs}} = V_s^{\mathrm{norm}}(1 + R_{\mathrm{LVL}}^{\mathrm{norm}}\eta), \tag{3}$$

where V_s^{norm} is the shear wave speed at 350 km evaluated from the PREM model [*Dziewonski and Anderson*, 1981].

Based on the interpretation of the normalized amplitude contrast $R_{\mathrm{LVL}}^{\mathrm{norm}}$, the reference velocity contrast η can introduce an error in the observed shear wave speed and eventually in the calculated melt volume fraction. If $R_{\mathrm{LVL}}^{\mathrm{norm}}$ is interpreted as a ratio of impedance contrasts across the LVL and the 410 km discontinuity, then η should be the impedance contrast across the 410 km discontinuity, approximately 0.09 for PREM [*Dziewonski and Anderson*, 1981]. If it is interpreted as the ratio of velocity contrasts, however, the appropriate η should also be the velocity contrast across the 410 km discontinuity, which is 0.03 for the PREM model. We chose to treat $R_{\mathrm{LVL}}^{\mathrm{norm}}$ as the ratio of velocity contrasts for analyzing Ps conversion data due to the sensitivity of the seismic data. We discuss the possible errors associated with this assumption in section 2.3.

ScS reverberation analysis yields impedance contrast (reflection coefficient) directly, and the results represent path-averaged quantities, so errors associated with the signal strength variations are smoothed out prior to our analysis. Thus, we do not normalize the impedance contrast atop the LVL with respect to the impedance contrast across 410. The nondimensional impedance contrast across the LVL, R_{LVL}, is given by

$$R_{\mathrm{LVL}} = \frac{\rho^{\mathrm{LVL}} V_S^{\mathrm{LVL}} - \rho^{\mathrm{top}} V_S^{\mathrm{top}}}{\rho^{\mathrm{top}} V_S^{\mathrm{top}}} < 0, \tag{4}$$

where ρ is the solid density and the superscripts "top" and "LVL" refer to values just above and just below the top of the LVL. Since there is no density jump due to phase change across the LVL, we can assume $\rho^{\mathrm{LVL}} \approx \rho^{\mathrm{top}}$,

then R_{LVL} becomes the velocity contrast across the top of the LVL, and we can again express the observed velocity as

$$V_s^{obs} = V_s^{norm}(1 + R_{LVL}). \quad (5)$$

2.1.2. Evaluating Temperature at Each Station

Mantle potential temperature influences the elastic moduli of the solid, thus controlling the shear wave speed. It is, therefore, crucial to understand the lateral variations in potential temperature in order to quantify lateral variations in melting. One observed parameter that allows us to constrain the potential temperature above each station is the depth to the top of the MTZ. For both Hawaii and the Coral Sea data sets, we use the temperature-sensitive depth to the 410 km discontinuity to evaluate the potential temperature at each station or corridor. Compared to the global average of 418 km [e.g., *Lawrence and Shearer*, 2008], this phase boundary is depressed in regions warmer than average and is elevated in regions that are colder. We use the deviation of the observed topography along the top of the MTZ beneath each station or corridor from the regional average z_{410} to calculate the deviation from a reference mantle potential temperature, T_0, at that station. The potential temperature, T, at each station is then given as

$$T = T_0 + \frac{1}{\gamma}\frac{dP}{dz}(z - z_{410}), \quad (6)$$

where γ is the Clapeyron slope for the olivine-wadsleyite phase transition, dP/dz is 36.67 MPa/km [*Katsura et al.*, 2004], and z is the observed depth to the top of the MTZ in kilometers. We use values of z_{410} as 435 km beneath Hawaii [*Courtier et al.*, 2007a] and 420 km beneath the Coral Sea [*Courtier and Revenaugh*, 2007]. The Clapeyron slope, γ, for the olivine-wadsleyite transition also influences the estimate of potential temperature at individual stations and, consequently, the calculated melt volume fraction. Laboratory measurements of γ from *Katsura et al.* [2004] predict a slope of 4 MPa/K which translates to a thermal gradient of roughly 10 K/km. In the data set from Hawaii, such a thermal gradient leads to unrealistically large lateral temperature variations. We therefore chose to use a lower Clapeyron slope of 3.1 MPa/K, as suggested by *Houser and Williams* [2010]. We treat the uncertainty in the Clapeyron slope as another source of error in our calculations. The treatment of this error is discussed in section 2.3.

We define regionally averaged quantities, indicating the averaged value over the stations in a given study area, by placing them within $\langle\rangle$. For example, the regionally averaged potential temperature $\langle T \rangle$ is determined from T calculated by taking average of T from each station obtained from equation (6).

2.2. Calculating Melt Volume Fraction From Observed Shear Wave Speed

In deciphering melt composition from the seismic observations, it is useful to define the anomaly function, ξ, which arises from the influence of melting. We obtain the observed shear wave speed V_S^{obs} at each station by using either equation (3) or (5). We also assign, for each station, a reference mantle shear wave speed V_S^{ref} and define the anomaly function as

$$\xi = \frac{V_S^{obs}}{V_S^{ref}}. \quad (7)$$

The schematic diagram in Figure 1 outlines the key parameters associated with each term in equation (7). There are five components—four prescribed and one unknown—in the governing equation (7). The reference mantle shear wave speed V_S^{ref} depends on the bulk solid composition, X, and the reference potential temperature, T_0, while the melting function ξ depends on melt wetting angle, θ, melt composition, and melt volume fraction, ϕ. This function must also satisfy the condition that $\xi \rightarrow 1$ as the melt volume fraction $\phi \rightarrow 0$. These three components are incorporated into ξ via an averaging scheme which is based on the microstructure of the melt. In this model, we do not account for changes in the melt distribution induced by deformation or chemical reaction [*Hier-Majumder*, 2011; *King et al.*, 2011; *Takei and Hier-Majumder*, 2009]. Next, we discuss the averaging scheme and the underlying microgeodynamic models.

2.2.1. A Formulation for the Melting Anomaly Function

In this work, we employ the averaging scheme of *Takei* [2002] to forward model the predicted shear wave speed, V_S^{pred}, as a function of the reference shear wave speed of the mantle, V_S^{ref}, as

$$V_S^{pred} = V_S^{ref}\sqrt{\frac{(1-\phi)(1-(1-\psi)^n)}{(\bar{\rho}/\rho)}}, \quad (8)$$

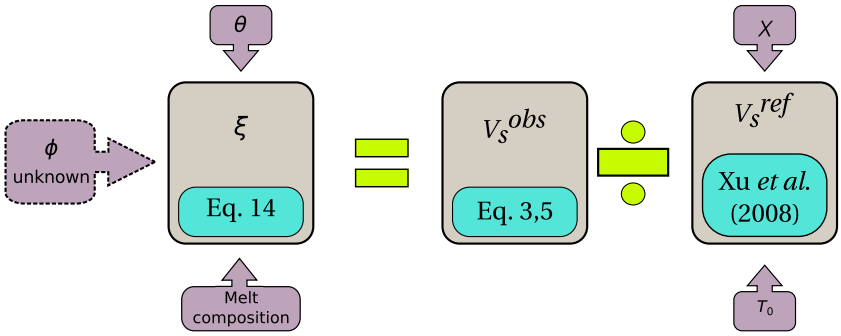

Figure 1. A schematic outline of the governing equation (7). The boxes with arrows indicate the input parameters, except for the box marked with the unknown, ϕ. The arrows also indicate the component of the governing equation that is influenced by the input parameter. The function ξ is described in equation (14). The source of the reference wave speed is the database of *Xu et al.* [2008], and the observed wave speeds are evaluated from observed amplitude and impedance contrasts by equations (3) and (5), respectively.

where $\bar{\rho}$ is the volume averaged density, ρ is the density of the solid, and ψ is the contiguity, the fractional area of intergranular contact, in the rock. The exponent n also depends on the contiguity ψ [*Takei*, 2002, Appendix A].

Contiguity of a partially molten aggregate depends both on the melt volume fraction and the dihedral angle of the melt [*von Bargen and Waff*, 1986; *Hier-Majumder et al.*, 2006; *Hier-Majumder and Abbott*, 2010; *Wimert and Hier-Majumder*, 2012]. Deformation of the matrix can expel melt from grain-edge tubules into grain boundary films, rendering the contiguity an anisotropic tensor [*Hier-Majumder*, 2011; *Hier-Majumder et al.*, 2004; *Takei and Holtzman*, 2009]. In this work, however, we ignore the anisotropic effects. It is a decreasing function of melt volume fraction and must satisfy two limits: $\psi \to 1$ as $\phi \to 0$, and $\psi \to 0$ as $\phi \to \phi_c$, where ϕ_c is the disaggregation melt fraction or rheologically critical melt fraction, at which grain surfaces are completely coated by the melt. Typical values of ϕ_c range between 20 vol % and 30 vol % [*Scott and Kohlstedt*, 2006; *Wimert and Hier-Majumder*, 2012; *Hier-Majumder et al.*, 2006]. We tested microgeodynamic models from a number of previous studies and report our results based on the model of *von Bargen and Waff* [1986]. Using the formulation of *von Bargen and Waff* [1986], we express the contiguity ψ as

$$\psi = \frac{2A_{gg}}{2A_{gg} + A_{gm}}, \tag{9}$$

where A_{gg} is the area of grain-grain contact, and A_{gm} is the area of grain-melt contact. For a given melt volume fraction ϕ and dihedral angle θ, the dimensionless areas are expressed as polynomial functions,

$$A_{gg} = \bar{A}_{gg} - b_{gg}\phi^p, \tag{10}$$

$$A_{gm} = b_{gm}\phi^p, \tag{11}$$

where $\bar{A}_{gg} \approx \pi$ is the difference between the grain boundary area of a dry system and the melt-bearing system [*Hier-Majumder and Abbott*, 2010]. The constants b and p are expressed as functions of the dihedral

Table 1. Constants Used in Equations Of State (EOS) to Calculate the Bulk Modulus of Melt[a]

Melt	K_0 (GPa)	ρ_0 kg/m^3	K'	Source
MORB	15.5	2590.0	7.2	*Guillot and Sator* [2007, Table 3]
Carbonated peridotite	24.9	2670.0	5.1	*Ghosh et al.* [2007, Figure 4]

[a]The values of P and K were obtained using the constants from the first two rows corresponding to the values of ρ/ρ_0 reported in the last row.

angle θ as [*von Bargen and Waff*, 1986]

$$\begin{Bmatrix} b_{gg} \\ b_{gm} \\ p_{gg} \\ p_{gm} \end{Bmatrix} = \begin{bmatrix} 1.03 \times 10^{-3} & -7.71 \times 10^{-2} & 8.16 \\ 1.00 \times 10^{-3} & -7.85 \times 10^{-2} & 12.86 \\ 8.66 \times 10^{-6} & 9.95 \times 10^{-4} & 0.424 \\ 2.41 \times 10^{-5} & 8.63 \times 10^{-5} & 0.43 \end{bmatrix} \begin{Bmatrix} \theta^2 \\ \theta \\ 1 \end{Bmatrix}. \tag{12}$$

Using the dihedral angle as an input parameter, and using equations (9)–(12), we evaluate ψ for equation (8). Next, requiring that the difference between the predicted and observed shear wave speeds is less than a preset tolerance ϵ, we set the criteria for numerically calculating melt volume fraction in the following way,

$$V_S^{obs} - V_S^{ref}\xi \leq \epsilon, \tag{13}$$

where

$$\xi = \sqrt{\frac{(1-\phi)(1-(1-\psi)^n)}{(\bar{\rho}/\rho)}}. \tag{14}$$

Notice as $\phi \to 0$, $\bar{\rho} \to \rho$, and according to equations (9)–(12), $\psi \to 1$, rendering $\xi \to 1$. In this case, melting is not required to explain the observed seismic signature.

2.2.2. Reference Mantle Properties

The reference mantle shear wave speed, V_S^{ref}, depends on the bulk solid composition, X, and the reference potential temperature T_0. To account for such a dependence, we evaluate the reference mantle properties from the database of *Xu et al.* [2008]. In their database, the bulk composition is parameterized by the volume fraction of the basaltic component, X, in the mantle. We use 10 different values of this fraction, ranging between 0.0 and 0.4. We also use 10 different values of the reference mantle potential temperature T_0 (a regional average from which temperatures at individual stations will be allowed to deviate) in equation (6), ranging between 1400 and 2300 K. In addition to the variations in solid composition and the reference potential temperature, we also vary the melt composition and dihedral angle, θ, leading to a total of 54,000 numerical experiments for 27 stations in Hawaii and 16,000 experiments for eight paths in the Coral Sea region.

For each value of basalt fraction, X, and reference potential temperature, T_0, we used a third-order polynomial to interpolate the reference mantle shear wave speed, V_S^{ref}, and density, ρ, atop the LVL for the inferred potential temperature at each station. The database of *Xu et al.* [2008] tabulates the physical properties on increments of 100 K. Since we allow the station potential temperatures to deviate from the reference potential temperature through equation (6), it is necessary to interpolate the reference properties for untabulated values of temperatures. To calculate the density of the melts, we use a Vinet equation of state (EOS) for a mid-ocean ridge basalt (MORB) melt from *Guillot and Sator* [2007] and a third-order Birch-Murnaghan EOS for a carbonated peridotite melt from *Ghosh et al.* [2007]. The parameters used in the EOS are listed in Table 1.

2.2.3. Numerical Solution

We solve the nonlinear governing equation (13) beneath each station for the unknown melt volume fraction ϕ, using a safe-root-search algorithm [*Press et al.*, 1992, chap. 9.4]. This algorithm combines two common nonlinear root finding methods, bisection and the Newton-Raphson method. During each solution step, we iterated until the convergence was less than a preset tolerance $\epsilon = 10^{-9}$. With an initial bracket of melt volume fraction between 1×10^{-6} and 0.1, it typically took ≤ 10 iterations to reach convergence. The calculations were carried out using the MuMaP suite, described above.

2.3. Error Analysis

The analysis in this work can introduce error through two parameters: the normalized velocity contrast, η, in equation (2) and the Clapeyron slope of olivine-wadsleyite transformation, γ, in equation (6). Using the method of error propagation [*Bevington and Robinson*, 2003, section 3.2], we can express σ_ϕ^2, the variance of the regional average melt volume fraction $\langle\phi\rangle$, as a function of errors arising from the measurement of γ and η

$$\sigma_\phi^2 = \sigma_\eta^2 \left(\frac{\partial\langle\phi\rangle}{\partial\eta}\right)_\gamma^2 + \sigma_\gamma^2 \left(\frac{\partial\langle\phi\rangle}{\partial\gamma}\right)_\eta^2, \tag{15}$$

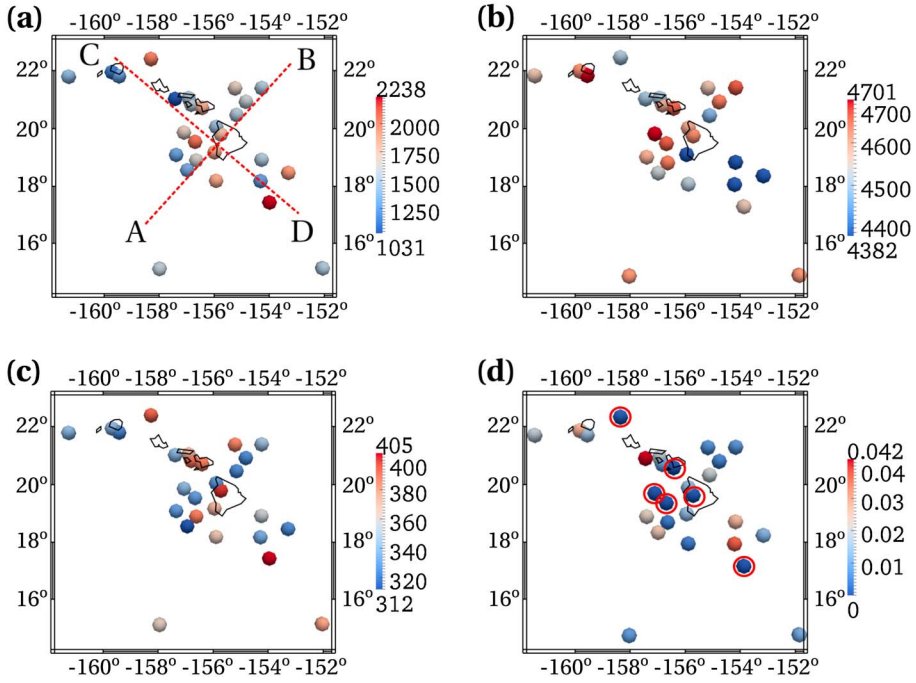

Figure 2. Maps of (a) calculated potential temperature, T, (b) observed seismic speed V_S^{obs}, (c) observed depth to the top of the LVL, and (d) calculated melt volume fraction beneath Hawaiian seismic stations. Each sphere is centered at the station location. The color of each sphere corresponds to the magnitude of the quantity according to the adjacent color scales. The spheres enclosed within red circles in Figure 2d register zero melt volume fraction. The results correspond to a dihedral angle of 10°, basalt fraction of 0.2, and a reference potential temperature of 1800 K. The regionally averaged melt volume fraction from the map in Figure 2d is 1.1 ± 0.8 vol %.

where σ^2 represents the variance of the quantity appearing in the subscript. The partial derivatives represent variations in the calculated value of $\langle\phi\rangle$ due to variations in the source of error (η and γ).

We calculated the standard deviation, which is the square root of the right-hand side in equation (15), of $\langle\phi\rangle$ for constant values of basalt fraction 0.2, reference potential temperatures 1800 K (Hawaii) and 1500 K (Coral Sea), and a dihedral angle of 10°, for a melt of basaltic composition, using the error propagation equation (15). The derivatives in equation (15) were calculated numerically. We carried out a total of 100 error tests for 10 different values of η between 0.01 and 0.1 and 10 different values of γ between 2.5 MPa/K and 4 MPa/K in the error analysis. For each of these tests, we calculated the regional average melt volume fraction by averaging the calculated melt volume fraction at each station. The resulting standard deviation σ_ϕ was 7.9×10^{-3} for Hawaii and 4.5×10^{-5} for the Coral Sea. In the Coral Sea data, the standard deviation is smaller, as the impedance contrast in equation (5) does not contain η, and the first quantity on the right-hand side of equation (15) does not contribute to the error.

3. Results

3.1. Lateral Variations in Melt Fraction

The results calculated from the seismic observations indicate lateral variations in temperature and observed shear wave speed. The maps in Figure 2 depict the variations in some observed and calculated quantities for the individual locations across Hawaiian region: potential temperature (Figure 2a), observed shear wave speed at the LVL (V_S^{obs}; Figure 2b), depth to LVL (Figure 2c), and melt volume fraction (Figure 2d). All maps correspond to a basalt fraction of 0.2, reference potential temperature of 1800 K, and a melt dihedral angle of 10°. The warmest mantle potential temperatures are mostly encountered underneath the Big Island and to the south. The scatter in the calculated potential temperatures in Figure 2a arises from the variations in the seismically observed MTZ topography. The observed shear wave speed at the LVL, V_S^{obs}, is lowest southeast of the Big Island. A close examination between the spatial distribution of potential temperature in Figure 2a and V_S^{obs} in Figure 2b reveals a general decrease in the shear wave speed and increase in temperature toward the southeast, along the line marked C-D in Figure 2a. The depth to the LVL also displays large lateral variations among the stations, as depicted in the map in Figure 2c. Some of the stations located along

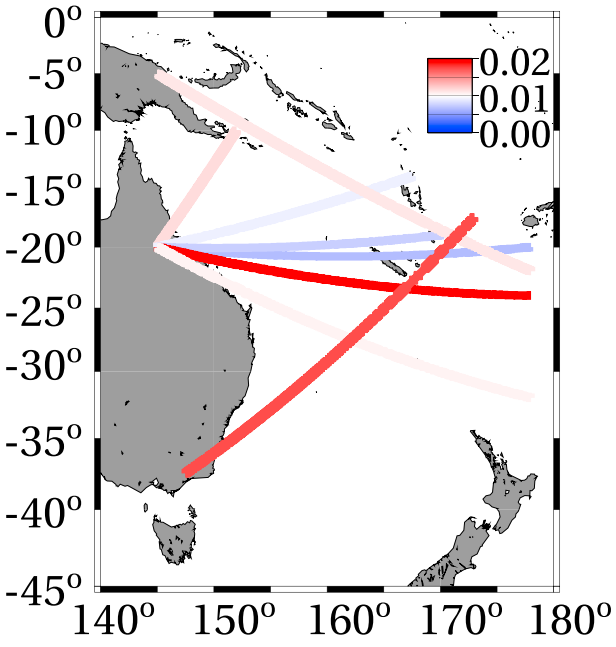

Figure 3. Map of calculated melt volume fraction underneath the Coral Sea. Lines indicate the trend and approximate location of each source-receiver geographic corridor. The color of each line corresponds to the magnitude of melt volume fraction. The calculated melt volume fraction corresponds to a dihedral angle of 10°, basalt fraction of 0.2, and a reference potential temperature of 1500 K for the Coral Sea. The regionally averaged melt volume fraction in this map is 1.2 ± 0.005 vol %.

the southwest-northeast trending line marked as A-B in Figure 2a display the shallowest LVLs in this region. These stations also have significantly less variation in calculated potential temperature. Finally, the map of melt volume fraction in Figure 2d depicts several stations along the A-B trend that display the fastest shear wave speed and register zero melt fraction. The stations located southeast of the Big Island register the highest melt volume fractions. The melt fraction beneath the Hawaiian region, averaged over all stations in Figure 2d, is 1.1 ± 0.8 vol %.

The calculated melt content at the LVL also displays lateral variations beneath the Coral Sea. The lateral variations in the Coral Sea data, as depicted in Figure 3, are much more muted compared to the Hawaiian Islands, perhaps in part because the seismic results are geographically path-averaged quantities prior to being input to our model rather than results from individual geographic locations at the Hawaiian stations. The regional average melt volume fraction beneath the Coral Sea is 1.2 ± 0.005 vol %.

3.2. Effect of Melt Composition

The seismic signature arising from the two different melt compositions considered in our study are practically indistinguishable. In Figure 4a, we plot the calculated melt volume fraction as a function of the observed shear wave velocities, for a basalt volume fraction of 0.2, reference potential temperature T_0 = 1800 K for Hawaii and 1500 K for the Coral Sea, and dihedral angle of 10° for both regions. Two sets of symbols indicate calculated melt volume fractions using MORB and carbonated peridotite melts. As the overlap between data points for both melt composition indicates the calculated melt volume fraction, the seismic signature of the LVL is essentially insensitive to variations in melt composition for such small melt volume fractions.

Calculated station potential temperatures and depths to the 410 km discontinuity, displayed in Figures 4b and 4c, respectively, demonstrate the difference between the thermal structures of the two regions. The light-colored circles from the Coral Sea in Figure 4b display little variation from an average value of approximately 1500 K, as the depth to the top of the MTZ in Figure 4c display little variation from the regional average of 420 km. The corresponding variations in the data set from Hawaii, marked by darker symbols in Figures 4b and 4c, are much larger.

3.3. Effect of Potential Temperature and Bulk Composition

The reference shear wave speed, V_S^{ref}, displays a modest variation with the reference potential temperature in both study areas. As discussed in section 2, for a given reference potential temperature T_0, we calculate the potential temperature, T, at each station using equation (6). Subsequently, we interpolate the value of V_S^{ref} at each station from the tabulated values in *Xu et al.* [2008]. Each data point in Figures 5a and 5b represents the average, $\langle V_S^{\mathrm{ref}} \rangle$, over the entire region for a reference basalt fraction of 0.2 and a dihedral angle of 10° for a given reference potential temperature. The horizontal line indicates the regionally averaged observed shear wave speed, $\langle V_S^{\mathrm{obs}} \rangle$. As the reference potential temperature is increased from 1400 K to 2300 K, $\langle V_S^{\mathrm{ref}} \rangle$ decreases by 400–500 m/s in both study regions. The inferred regionally averaged melt volume fractions,

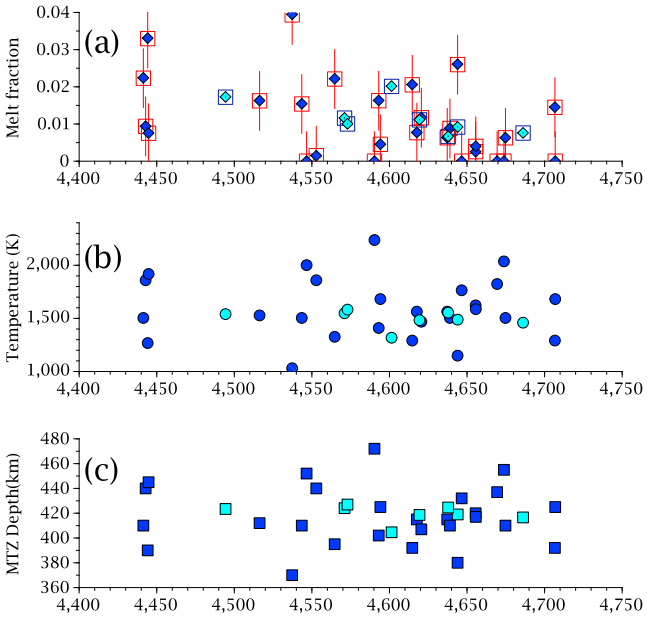

Figure 4. Plots of (a) calculated melt volume fraction, (b) potential temperature, and (c) observed topography as a function of observed shear wave speed for all results in this study. In Figure 4a the filled symbols represent melt fraction calculated using a MORB EOS, while the open symbols represent melt volume fractions calculated using a carbonated peridotite EOS. The vertical bars in Figure 4a represent the range of error within $\pm 1\sigma$ interval. The error bars for the data from the Coral Sea is smaller than the symbols. The filled light-colored symbols represent data from the Coral Sea, while the dark, filled symbols represent data from the Hawaiian Islands in Figures 4b and 4c. In this data set, the dihedral angle is 10°, reference potential temperature is 1800 K for Hawaiian Islands and 1500 K for the Coral Sea region, and the reference basalt fraction is 0.2.

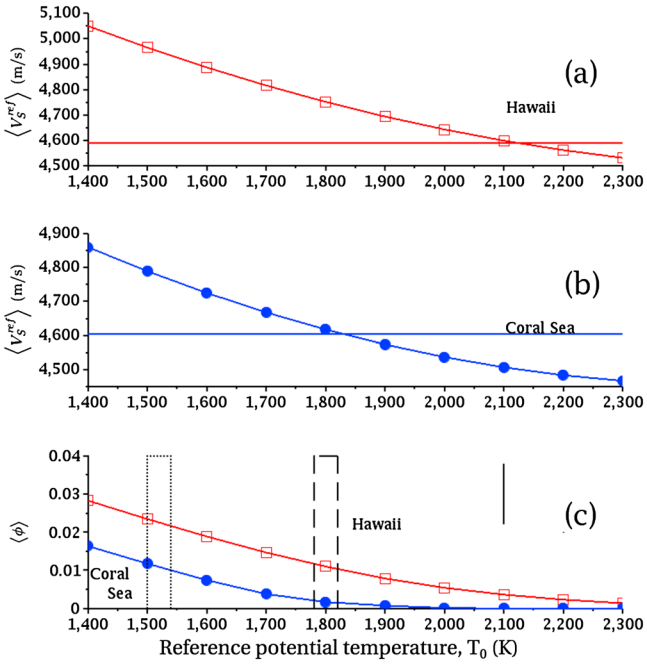

Figure 5. (a) Regionally averaged reference shear wave speed, $\langle V_S^{\text{ref}} \rangle$, as a function of reference potential temperature T_0 from the Hawaiian Islands. The horizontal line represents the regionally averaged observed shear wave speed, $\langle V_S^{\text{obs}} \rangle$. (b) The same plot as in Figure 5a for the Coral Sea region. (c) Regional average of calculated melt volume fraction as a function of the reference potential temperature for both regions. Filled circles represent data from the Coral Sea, and open squares represent data from the Hawaiian Islands. The height of the vertical bar to the right indicates the error bar for each data point from Hawaii within a $\pm 1\sigma$ range. All plots correspond to a dihedral angle of 10° and a reference basalt fraction of 0.2. Width of the rectangles indicate the likely range of potential temperatures in the two regions.

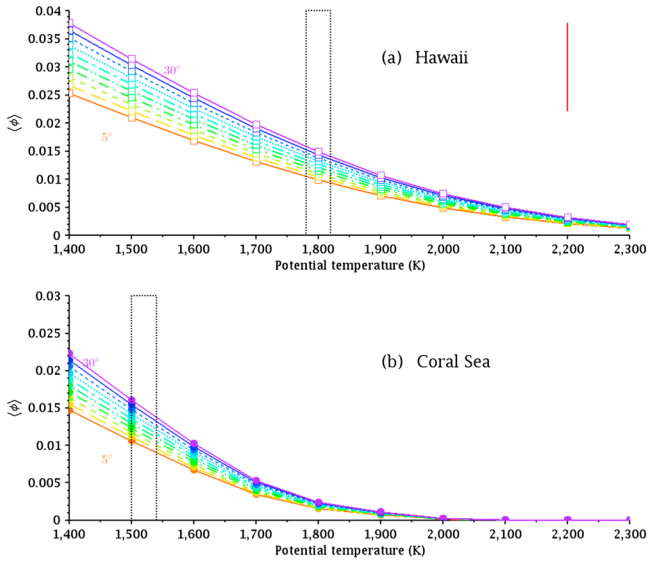

Figure 6. Plot of calculated regionally averaged melt volume fraction, $\langle\phi\rangle$, as a function of reference potential temperature T_0 for 10 different values of the dihedral angles. The maximum and minimum dihedral angles in the range are annotated on the plot. The data correspond to a basalt fraction of 0.2 in the bulk composition. The data points represent regional averages from (a) the Hawaiian Islands and (b) the Coral Sea. Width of the rectangles indicate the likely range of potential temperatures in the two regions. The width of the vertical bar in Figure 6a is $\pm 1\sigma$ and represents the range of error associated with each data point. The magnitude of error in Figure 6b is smaller than the symbols.

$\langle\phi\rangle$, for both regions are plotted as a function of the reference potential temperature in Figure 5c. The vertical rectangles indicate the expected average potential temperature in each study area. The overall variation in melt volume fraction is approximately 2.8 vol % in Hawaii and 1.6 vol % in the Coral Sea. The vertical bar in Figure 5c (right) represents the error associated with each data point from the Hawaiian Islands within a $\pm 1\sigma$ range. For likely reference potential temperatures of 1800 K (Hawaii) and 1500 K (Coral Sea), both regions register average values of approximately 1 vol % melt.

The series of plots in Figure 6 demonstrate the variation in calculated regionally averaged melt volume fraction, $\langle\phi\rangle$, as a function of reference potential temperatures for Hawaii in Figure 6a and the Coral Sea in Figure 6b. The width of the rectangle in both plots indicate the range of likely potential temperature in each of the regions, based on petrological evidence (summarized by *Courtier et al.* [2007b]). The vertical line in Figure 6a represents the error associated with each data point in the Hawaiian Islands. The trend in Figure 6a is similar to that in Figure 5c. Upward shifting of the curves with an increase in the dihedral angle arises from the trade-off (negative correlation) between melt volume fraction and dihedral angle. The distance between the different curves narrows at higher reference potential temperature indicating that this trade-off is less effective at smaller melt volume fractions. At any given reference potential temperature, the variation in $\langle\phi\rangle$ with the dihedral angle is relatively modest. For example, in Hawaii, for a potential temperature of 1800 K, the value of $\langle\phi\rangle$ varies between 0.9 vol % and 1.4 vol % with the variations in the dihedral angle. For the data from the Coral Sea in Figure 6b, at a potential temperature of 1500 K, the value of $\langle\phi\rangle$ varies between 1 vol % and 1.6 vol % for the same variation in dihedral angle. Thus, the influence of the wetting angle on the inferred melt volume fraction is modest but discernible by the technique used in this work.

The regionally averaged melt volume fraction, $\langle\phi\rangle$, displays little variation as a result of varying the basalt fraction in the bulk composition. The plots in Figure 7 depict the variations for both study regions for dihedral angles ranging between 5° and 30°, as annotated in the plots. The height of the vertical bar in Figure 7a represents the $\pm 1\sigma$ range for each data point. The corresponding error bar is smaller than the symbol sizes in Figure 7b. The reference potential temperatures in the plots are 1800 K for Hawaii and 1500 K for the Coral Sea region. In both regions, the melt volume fraction remains nearly unchanged with bulk basalt fraction for any given dihedral angle.

One complexity in the reference composition arises from a solid-state phase transition in the bulk composition. This opx-C2/c phase transition takes place around the depth of 340 km and depends strongly on the basalt fraction in the solid composition [*Xu et al.*, 2008]. Based on the equilibrium assemblage data of

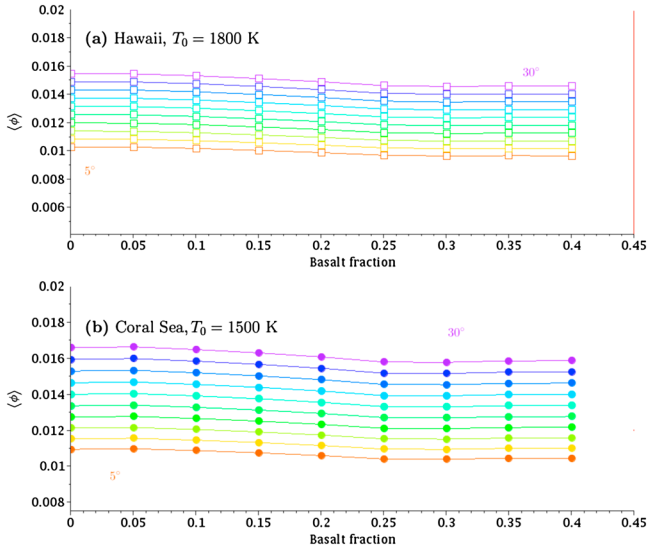

Figure 7. Plot of regionally averaged melt volume fraction $\langle\phi\rangle$ as a function of the basalt fraction in the bulk composition for 10 different values of dihedral angles. Annotations in each plot indicate the corresponding reference potential temperature. The data represent regional averages from (a) the Hawaiian Islands and (b) the Coral Sea region. The width of the vertical bar in Figure 7a is $\pm 1\sigma$ and represents the range of error associated with each data point. The magnitude of error in Figure 7b is smaller than the symbols.

Xu et al. [2008], this transition is observed only for $X = 0.18$ at the depth (352 km) and the range of potential temperatures observed in this study. This phase transition leads to a small, $\mathcal{O}(10^{-3})$, fractional increase in the reference shear wave speed at $X = 0.18$ compared to $X = 0.15$ and $X = 0.2$. The faster reference shear wave speed leads to a slightly higher ($\sim$ 0.1 vol %) regionally averaged melt fraction at $X = 0.18$ compared to $X = 0.15$ and $X = 0.2$. Since this phase transition appears for just one composition and has a relatively small influence on the calculated melt volume fraction, we chose not to report the data point corresponding to $X = 0.18$ in Figure 7. We note, however, that if present, the effect of this transition on the inferred melt volume fraction is much smaller than the temperature and dihedral angle trade-offs discussed earlier.

4. Discussions

4.1. The Nature of the LVL

The seismic signature from the two study regions indicate similar melt volume fractions and depths to the LVL. For a given basalt fraction (0.2), and dihedral angle (10°), the LVL beneath Hawaii contains an average of 1.1 $\pm$ 0.8 vol % partial melt for a regional potential temperature of 1800 K, while that beneath the Coral Sea contains a regional average of 1.2 $\pm$ 0.005 vol % melt for a regional potential temperature of 1500 K. The similarity of the melt volume fraction between these two different tectonic settings suggests that melting in the LVL is not suppressed underneath mantle plumes. This observation, similar to that of *Tauzin et al.* [2010], contradicts the prediction of the water filter model of *Bercovici and Karato* [2003]. In addition, the average LVL depth is 355 km under the Hawaiian Islands and 352 km under the Coral Sea, within the error of the seismic methods (5–10 km). The onset of carbon-induced melting should take place at greater depths beneath both mantle plumes and in subduction zones [*Dasgupta and Hirschmann*, 2010], also contrary to our observation. While a detailed petrologic model is beyond the scope of this work, these constraints from our observations can aid future models of volatile-induced melting in the LVL. It is important to emphasize that our results do not contradict the presence of volatile-bearing melts in the LVL. In contrast, as the electrical conductivity calculations in the following section indicates, electrical conductivity observations and our calculations are best matched by a silicate melt containing a small amount of dissolved volatiles.

As discussed in the context of the results, the technique reported in this work is able to quantify the influence of the test parameters to melt fractions as small as $<$ 1 vol % of melting. Despite this high resolution, the predicted shear wave speed reductions are insensitive to the composition of the melt. The insensitivity arises from (a) the relative similarity of the bulk modulus and density of MORB and carbonated peridotite melts and (b) the modest contribution of the melt bulk modulus to the effective bulk modulus, since the melt volume fraction is only $\mathcal{O}(0.01)$. In the next section, we use the calculated melt volume fraction from

the seismic signature to predict the electrical conductivity of the LVL and compare it with the observations in the Pacific.

4.2. Constraints From Electrical Conductivity

MORB and carbonated peridotite melts, as Figure 4 depicts, are equally effective in reducing the shear wave speed. The calculated melt volume fraction for each station remains practically unchanged for these two melt compositions. When compared with observed electrical conductivity, however, the results begin to provide additional constraints on the possible composition of the melt.

A number of studies explore the upper mantle electrical conductivity profile in the North Pacific [*Shimizu et al.*, 2010a, 2010b; *Utada et al.*, 2003; *Lizarralde et al.*, 1995]. The long-period magnetotelluric measurements by *Lizarralde et al.* [1995] indicate the presence of a highly conductive zone between the depths of 150 and 400 km, characterized by electrical conductivities of 0.05 to 0.1 S/m. A number of subsequent conductivity maps of the North Pacific in 1-D and 3-D suggest an electrical conductivity of $<$ 0.01 S/m at a depth of 350 km. Despite the variations, the results from these studies provide an upper limit to the electrical conductivity of the LVL, corresponding to our inferred melt volume fractions.

We combine our estimates of melt volume fraction with laboratory measurements of effective electric conductivity by using Archie's Law,

$$\bar{\sigma} = C\phi^q \sigma_m, \tag{16}$$

where $\bar{\sigma}$ is the effective electrical conductivity, C and q are constants, ϕ is the melt volume fraction, and σ_m is the electrical conductivity of the melt. Using the values of constants for olivine-MORB aggregate of *ten Grotenhuis et al.* [2005] and olivine-carbonatite from *Yoshino et al.* [2010], and our regional average of $\phi = 0.01$, we obtain an effective electrical conductivity of 0.03 S/m for olivine-MORB and 0.5 S/m for olivine-carbonatite aggregates. The effective electrical conductivity of this 100% carbonatite-bearing aggregate is substantially higher than the highest observed values of electrical conductivity for our inferred melt volume fraction. For smaller, more realistic, amounts of dissolved volatiles—hydrous or carbonate—the conductivity of the melt will be less. Such melts of predominant silicate composition are better suited to explain the observed seismic anomaly while predicting an effective conductivity within the bounds of the observed values.

In a recent work, *Mookherjee et al.* [2008] calculate the electrical conductivity of hydrous silicate melts as a function of dissolved water. For our melt volume fraction and an olivine conductivity of $10^{-2.2}$ s/m [*Yoshino et al.*, 2010], the effective electrical conductivity of the aggregate varies between 0.01 S/m for 1% water in the melt and 0.07 S/m for 3% water in the melt, a better match with the observed electrical conductivity. Similar measurements for carbonate-bearing melts, with a systematic variation in the dissolved carbonate content, will be extremely useful in understanding the nature of volatile-assisted melting in the LVL.

5. Conclusion

In this work, we analyze the seismic signature of an LVL in the deep upper mantle from two different tectonic settings. In both regions, the LVL occurs at an approximate depth of 350 km and contains approximately 1 vol % melt. The seismic signature arising from the melt volume fraction trades off with the regional temperature and dihedral angle. The bulk solid composition does not influence the melt volume fraction significantly. The seismic signature was insensitive to the melt composition. Compared with observed values of mantle electrical conductivity, it is unlikely that the LVL contains purely carbonatitic melts, but a silicate melt with a small amount of dissolved volatiles does not contradict our seismic constraints.

Acknowledgments

This work was supported by Research Corporation grant 19722 (AMC), the James Madison University Program of grants for Faculty Assistance (AMC), and NSF grant EAR0911094 (SH-M). The authors also appreciate input from Ved Lekić and Garrett Leahy during early stages of the manuscript. Insightful and thorough reviews by two anonymous reviewers greatly improved the manuscript.

References

Bercovici, D., and S. Karato (2003), Whole-mantle convection and the transition zone water filter, *Nature*, *425*, 39–44.

Bevington, P. R., and D. K. Robinson (2003), *Data Reduction and Error Analysis for Physical Sciences,* 3rd ed., McGraw Hill, Univ. of Calif.

Courtier, A. M., and J. Revenaugh (2007), Deep upper-mantle melting beneath the Tasman and Coral Seas detected with multiple *ScS* reverberations, *Earth Planet. Sci. Lett.*, *259*, 66–76.

Courtier, A. M., B. Bagley, and J. Revenaugh (2007a), Whole mantle discontinuity structure beneath Hawaii, *Geophys. Res. Lett.*, *34*, L17304, doi:10.1029/2007GL031006.

Courtier, A. M., et al. (2007b), Correlation of seismic and petrologic thermometers suggests deep thermal anomalies beneath hotspots, *Earth Planet. Sci. Lett.*, *264*, 308–316.

Dasgupta, R., and M. M. Hirschmann (2010), The deep carbon cycle and melting in Earth's interior, *Earth Planet Sci. Lett.*, *298*, 1–13.

Dziewonski, A. M., and D. L. Anderson (1981), Preliminary reference Earth model, *Phys. Earth Planet. In.*, *25*, 297–356.
Gao, W., E. Matzel, and S. Grand (2006), Upper mantle seismic structure beneath eastern Mexico determined from *P* and *S* waveform inversion and its implications, *J. Geophys. Res.*, *111*, B08307, doi:10.1029/2006JB004304.
Ghosh, S., E. Ohtani, K. Litasov, A. Suzuki, and T. Sakamaki (2007), Stability of carbonated magmas at the base of the Earth's upper mantle, *Geophys. Res. Lett.*, *34*, L22312, doi:10.1029/2007GL031349.
Guillot, B., and N. Sator (2007), A computer simulation study of natural silicate melts. Part II: High pressure properties, *Geochim. Cosmochim. Ac.*, *71*, 4538–4556.
Hier-Majumder, S. (2008), Influence of contiguity on seismic velocities of partially molten aggregates, *J. Geophys. Res.*, *113*, B12205, doi:10.1029/2008JB005662.
Hier-Majumder, S. (2011), Development of anisotropic mobility during two-phase flow, *Geophys. J. Int.*, *186*, 59–68.
Hier-Majumder, S., and M. E. Abbott (2010), Influence of dihedral angle on the seismic velocities in partially molten rocks, *Earth Planet. Sci. Lett.*, *299*, 23–32.
Hier-Majumder, S., and A. Courtier (2011), Seismic signature of small melt fraction atop the transition zone, *Earth Planet. Sci. Lett.*, *308*, 334–342.
Hier-Majumder, S., P. Leo, and D. Kohstedt (2004), On grain boundary wetting during deformation, *Acta Mater.*, *52*, 3425–3433.
Hier-Majumder, S., Y. Ricard, and D. Bercovici (2006), Role of grain boundaries in magma migration and storage, *Earth Planet. Sci. Lett.*, *248*, 735–749.
Houser, C., and Q. Williams (2010), Reconciling Pacific 410 and 660km discontinuity topography, transition zone shear velocity patterns, and mantle phase transitions, *Earth Planet. Sci. Lett.*, *296*, 255–266.
Huckfeldt, M., A. Courtier, and G. M. Leahy (2013), Implications for the origin of Hawaiian volcanism from a converted wave analysis of the mantle transition zone, *Earth Planet. Sci. Lett.*, *373*, 194–204.
Jasbinsek, J., and K. Dueker (2007), Ubiquitous low-velocity layer atop the 410 km discontinuity in the northern Rocky Mountain, *Geochem. Geophys. Geosys.*, *8*, Q10004, doi:10.1029/2007GC001661.
Katsura, T., et al. (2004), Olivine-wadsleyite transition in the system $(Mg,Fe)_2SiO_4$, *J. Geophys. Res.*, *109*, B02209, doi:10.1029/2003JB002438.
King, D. S. H., S. Hier-Majumder, and D. L. Kohlstedt (2011), An experimental study of the effects of surface tension in homogenizing perturbations in melt fraction, *Earth Planet. Sci. Lett.*, *307*, 735–749.
Lawrence, J., and P. Shearer (2008), Imaging mantle transition zone thickness with SdS-SS finite-frequency sensitivity kernels, *Geophys. J. Int.*, *174*, 143–158.
Leahy, G., and D. Bercovici (2007), On the dynamics of a hydrous melt layer above the transition zone, *J. Geophys. Res.*, *112*, B07401, doi:10.1029/2006JB004631.
Lizarralde, D., A. Chave, G. Hirth, and A. Schultz (1995), Northeastern pacific mantle conductivity profile from long-period magnetotelluric sounding using Hawaii-to-California submarine cable data, *J. Geophys. Res.*, *100*, 17,837–17,854, doi:10.1029/95JB01244.
Mookherjee, M., L. Stixrude, and B. Karki (2008), Hydrous silicate melt at high pressure, *Nature*, *452*, 983–986.
Press, W. H., S. A. Teukolsky, W. T. Vetterling, and B. P. Flannery (1992), *Numerical Recipes in FORTRAN*, chap. 19.6, 2nd ed., Cambridge Univ. Press, Cambridge, U. K.
Revenaugh, J., and H. Jordan (1991), Mantle layering from *ScS* reverberations. 2: The transition zone, *J. Geophys. Res.*, *96*, 19,763–19,780.
Revenaugh, J., and S. Sipkin (1994), Seismic evidence for silicate melt atop the 410 km mantle discontinuity, *Nature*, *369*, 474–476.
Scott, T., and D. Kohlstedt (2006), The effect of large melt fraction on the deformation behavior of peridotite, *Earth Planet. Sci. Lett.*, *246*, 177–187.
Shimizu, H., T. Koyama, K. Baba, and H. Utada (2010a), Revised 1-D mantle electrical conductivity structure beneath the north Pacific, *Geophys. J. Int.*, *180*, 1030–1048.
Shimizu, H., H. Utada, K. Baba, T. Koyama, M. Obayashi, and Y. Fukao (2010b), Three-dimensional imaging of electrical conductivity in the mantle transition zone beneath the North Pacific Ocean by a semi-global induction study, *Phys. Earth Planet. Int.*, *183*, 252–269.
Song, T., D. Helmberger, and S. Grand (2004), Low-velocity zone atop the 410 km seismic discontinuity in the northwestern United States, *Nature*, *427*, 530–533.
Takei, Y. (2002), Effect of pore geometry on v_p/v_s: From equilibrium geometry to crack, *J. Geophys. Res.*, *107*, 2043, doi:10.1029/2001JB000522.
Takei, Y., and S. Hier-Majumder (2009), A generalized formulation of interfacial tension driven fluid migration with dissolution/precipitation, *Earth Planet. Sci. Lett.*, *288*, 138–148.
Takei, Y., and B. K. Holtzman (2009), Viscous constitutive relations of solid-liquid composites in terms of grain boundary contiguity: 1. Grain boundary diffusion control model, *J. Geophys. Res.*, *114*, B06205, doi:10.1029/2008JB005850.
Tauzin, B., E. Debayle, and G. Wittlinger (2010), Seismic evidence for a global low-velocity layer within the Earth's upper mantle, *Nature*, *3*, 718–721, doi:10.1038/NGEO969.
ten Grotenhuis, S., M. Drury, C. Spiers, and C. J. Peach (2005), Melt distribution in olivine rocks based on electrical conductivity experiments, *J. Geophys. Res.*, *110*, B12201, doi:10.1029/2004JB003462.
Utada, H., T. Koyama, H. Shimizu, and A. Chave (2003), A semi-global reference model for electrical conductivity in the mid-mantle beneath the north Pacific region, *Geophys. Res. Lett.*, *30*, 1194, doi:10.1029/2002Gl016092.
Vinnik, L., and V. Farra (2007), Low S velocity atop the 410 km discontinuity and mantle plumes, *Earth Planet. Sci. Lett.*, *262*, 398–412, doi:10.1016/j.epsl.2007.07.051.
von Bargen, N., and H. Waff (1986), Permeabilities, interfacial areas and curvatures of partially molten systems: Results of numerical computations of equilibrium microstructures, *J. Geophys. Res.*, *91*, 9261–9276.
Wimert, J. T., and S. Hier-Majumder (2012), A three-dimensional microgeodynamic model of melt geometry in the Earth's deep interior, *J. Geophys. Res.*, *117*, B04203, doi:10.1029/2011JB009012.
Xu, W., C. Lithgow-Bertolini, L. Stixrude, and J. Ritsema (2008), The effect of bulk composition and temperature on mantle seismic structure, *Earth Planet Sci. Lett.*, *275*, 70–79.
Yoshino, T., M. Laumonier, E. McIsaac, and T. Katsura (2010), Electrical conductivity of basaltic and carbonatite melt-bearing peridotites at high pressures: Implications for melt distribution and melt fraction in the upper mantle, *Earth Planet. Sci. Lett.*, *295*, 593–602.